Modeling of Inclusion Removal in Ladle Refining

Jun Aoki, Lifeng Zhang and Brian G. Thomas
Dept. of Mechanical & Industrial Engineering
University of Illinois at Urbana-Champaign
1206 West Green Street
Urbana, IL 61801
Tel.: 217-333-6919 Fax: 217-244-6534
E-mail: junaoki@uiuc.edu, zhang25@uiuc.edu, bgthomas@uiuc.edu

Key words: Steelmaking, Ladle refining, Clean steel, Gas injection, Multiphase flow, Inclusion, Bubble, Attachment probability

INTRODUCTION

Gas injection is widely used in secondary refining processes to homogenize chemical composition and temperature and to remove inclusions. It is an industrial requirement to minimize the size and concentration of inclusions in the product while minimizing production time to save energy and lessen refractory wear. Gas bubbling is effective to increase the cleanliness of steel mainly by two mechanisms. Firstly, gas bubbling creates the buoyant plume that generates the recirculation flow pattern in the ladle which enhances the transport of inclusions to the top surface, and turbulent mixing with the slag layer to remove the inclusions. Secondly, many inclusions collide with the bubbles and are carried quickly to the top surface, owing to the much higher floatation velocity of a gas bubble, relative to an inclusion.

In this study, inclusion removal by bubbles is modeled in three steps. Firstly, the flow pattern induced by gas injection at the bottom of a ladle is calculated using an Eulerian-Lagrangian model of three-dimensional transient multiphase flow. The equations are solved with the commercial package FLUENT, with the help of extensive user defined subroutines developed by the authors. Secondly, the attachment of inclusions to an individual bubble is simulated in a micro-scale model that includes random turbulent motion, and the results of many thousands of simulations are analyzed statistically. The effect of turbulent kinetic energy on inclusion attachment probability is investigated for the first time. And thirdly, the inclusion removal rate is calculated by incorporating the inclusion attachment probability model into the macro-scale flow field obtained with the Eulerian-Lagrangian model, using a fully-coupled approach.

This work is a part of a larger project to develop comprehensive computational modeling tools for the quantitative study of metallurgical processes and for designing new processes such as continuous steelmaking[1-3]. In addition to improved understanding of cleanliness in current ladle refining processes, the modeling technology developed in this work will aid in the development and evaluation of these new processes.

MODEL 1. LADLE FLOW

An Eulerian-Lagrangian approach has been developed to model transient, multiphase turbulent flow of liquid metal flow and gas bubbling in three dimensions, and then applied to simulate a typical off-center bottom-stirred steel-refining ladle. The flow of the fluid phase is solved in an Eulerian frame of reference together with the motion of every individually injected bubble, solved in its own Lagrangian frame of reference. These calculations are performed simultaneously by coupling together the phase fraction and interaction forces such as the drag force and lift force. The method here is similar to that of Guo and Irons'[4], who successfully reproduced the flow field of the Wood's metal experiment with their own code, but has the advantage of running through a commercial software package.

Liquid Flow

For the liquid phase flow field, a single set of Navier-Stokes equations containing liquid volume fraction α_l is solved.

Continuity:

$$\frac{\partial}{\partial t}(\alpha_l \rho_l) + \nabla \cdot (\alpha_l \rho_l \underline{u}_l) = 0 \tag{1}$$

Momentum:

$$\frac{\partial}{\partial t}(\alpha_l \rho_l \underline{u}_l) + \underline{u}_l \cdot \nabla(\alpha_l \rho_l \underline{u}_l) = -\nabla p + \nabla \cdot [\alpha_l(\mu_l + \mu_t)]\nabla u_l + F_b \tag{2}$$

where F_b is the source term for momentum exchange with the bubbles, obtained as follows,

$$F_b = -\sum_i^{N_{b,cell}} \left[\frac{3\alpha_l \mu_l C_{D,i} \, \mathrm{Re}_i}{4 d_{b,i}^2 \rho_{b,i}}(\underline{u}_l - \underline{u}_{b,i}) + C_{VM} \frac{\alpha_l \rho_l}{\rho_{b,i}}\left(\frac{D_l}{Dt}u_l - \frac{D_b}{Dt}u_{b,i}\right) + C_L \frac{\alpha_l \rho_l}{\rho_{b,i}}(\underline{u}_l - \underline{u}_{b,i}) \times \nabla \times \underline{u}_l + \frac{\alpha_l \rho_l}{\rho_{b,i}}\underline{u}_l \cdot \nabla \underline{u}_l \right] Q_{b,i}^s \Delta t \tag{3}$$

where $N_{b,cell}$ is the number of bubbles in the computational cell, u is velocity, d is diameter, μ is viscosity, and ρ is density. The subscript b,i means the "ith bubble", subscript l means liquid, and the underline means vector. $Q_{b,i}^s$ is the flow rate (kg/s) of the injected bubble stream, and Δt is the time step of bubble trajectory calculation. $\frac{D_l}{Dt}$ and $\frac{D_b}{Dt}$ are total derivatives with respect to the liquid and bubble phases. Re is the particle Reynolds number which is defined in terms of the relative velocity between the fluid and the particle as follows:

$$\mathrm{Re} = \frac{\rho_l d_{b,i} |\underline{u}_l - \underline{u}_{b,i}|}{\mu_l} \tag{4}$$

C_D, C_{VM} and C_L are the drag coefficient, the virtual mass coefficient, and the lift coefficient described in bubble motion section. μ_t in eq. (2) is the turbulent viscosity, which is defined as

$$\mu_t = C_\mu \rho_l \frac{k^2}{\varepsilon} \tag{5}$$

Turbulence
The standard k-ε model is used to model turbulence, which means that the following transport equations of k and ε are solved.

$$\alpha_l \rho_l \left(\frac{\partial k}{\partial t} + \underline{u}_l \cdot \nabla k\right) = \nabla \cdot \left(\alpha_l \frac{\mu_t}{\sigma_k}\nabla k\right) + \alpha_l G_k - \alpha_l \rho_l \varepsilon + S_k \tag{6}$$

$$\alpha_l \rho_l \left(\frac{\partial \varepsilon}{\partial t} + \underline{u}_l \cdot \nabla \varepsilon\right) = \nabla \cdot \left(\alpha_l \frac{\mu_t}{\sigma_\varepsilon}\nabla \varepsilon\right) + \alpha_l C_1 \frac{\varepsilon}{k} G_k - \alpha_l C_2 \rho \frac{\varepsilon^2}{k} \tag{7}$$

$$G_k = \mu_t \left(\frac{\partial u_{l,i}}{\partial x_j} + \frac{\partial u_{l,j}}{\partial x_i}\right)\frac{\partial u_{l,i}}{\partial x_j} \tag{8}$$

The values of the constants are C_μ=0.09, C_1=1.44, C_2=1.92, σ_k=1.0, and σ_ε=1.3.
S_k in eq. (6) is the source of turbulent kinetic energy due to the shear force and wake formation by bubble. S_k is assumed to be proportional to the product of the drag force and relative velocity.[5]

$$S_k = \frac{C_{sk}}{\Delta V_{cell}} \sum_i^{N_{b,cell}} \frac{3\alpha_l \mu_l C_{D,i} \, \mathrm{Re}_i}{4 d_{b,i}^2 \rho_{b,i}} |\underline{u}_l - \underline{u}_{b,i}|^2 Q_{b,i}^s \Delta t \tag{9}$$

where ΔV_{cell} is the computational cell volume and C_{sk} is a constant. The value of C_{sk} is set to 0.12 by matching the calculated flow field with the experimental data by Xie and Oeters[6], as explained in the Validation section.

Bubble Motion
The motion of each bubble through the liquid velocity field is calculated by integrating the following transport equation.

$$\frac{d\underline{u}_{b,i}}{dt} = \frac{3\mu_l C_D \, \mathrm{Re}}{4\rho_{b,i} d_{b,i}^2}(\underline{u}_l - \underline{u}_{b,i}) + \frac{(\rho_{b,i} - \rho_l)}{\rho_{b,i}}g\underline{e}_y + C_{VM}\frac{\rho_l}{\rho_{b,i}}\frac{d}{dt}(\underline{u}_l - \underline{u}_{b,i}) + C_L \frac{\rho_l}{\rho_{b,i}}(\underline{u}_l - \underline{u}_{b,i}) \times \nabla \times \underline{u}_l + \frac{\rho_l}{\rho_{b,i}}\underline{u}_l \cdot \nabla \underline{u}_l \tag{10}$$

The terms on the right hand side represent the drag force, the buoyancy force, the virtual mass force, the lift force, and the pressure gradient force. The coefficients C_D, C_{VM} and C_L are the drag, virtual mass, and lift coefficients.

The drag coefficient C_D is from Kuo and Wallis[7], which takes bubble shape change into account according to its diameter.

$$C_D = \frac{16}{\text{Re}} \qquad \text{Re} < 0.49$$

$$C_D = \frac{20.68}{\text{Re}^{0.643}} \qquad 0.49 < \text{Re} < 100$$

$$C_D = \frac{6.3}{\text{Re}^{0.385}} \qquad 100 < \text{Re} \tag{11}$$

$$C_D = \frac{\text{We}}{3} \qquad \text{Re} > \frac{2065.1}{\text{We}^{2.6}}$$

$$C_D = \frac{8}{3} \qquad \text{We} > 8$$

We is the Weber number defined as follows.

$$\text{We} = \frac{\rho_l d_{b,i} \left| \underline{u}_l - \underline{u}_{b,i} \right|^2}{\sigma_{lb}} \tag{12}$$

where σ_{lb} is the surface tension between liquid and bubble. The terminal velocity of the bubble calculated using the drag coefficient from eq. (11) is shown in Figure 1. The slope of the terminal velocity changes with bubble size according to the shape change of the bubble, which adopts sphere, spheroid, and spherical cap shapes for small, intermediate, and large bubble size respectively (Figure 2). The virtual mass coefficient C_{VM} is set to 0.5, which is the theoretical value of a spherical object moving in a fluid.
For the lift coefficient C_L, the following empirical relationship by Beyerlein et al.[8] is used.

$$C_L = 0.00165 \alpha_b^{-0.78} \tag{13}$$

where α_b is the bubble volume fraction.
The trajectories of the bubbles are obtained by integrating eq. (10).

$$\underline{x}_{b,i} = \int \underline{u}_{b,i} dt \tag{14}$$

The effect of turbulence on bubble trajectories is incorporated with the "random walk" method. A fluctuating velocity component is added to the liquid velocity in eq.(10), which varies in proportion to the local turbulence level using a random number ς with normal Gaussian distribution,

$$\underline{u}_l = \overline{\underline{u}_l} + \varsigma \sqrt{\frac{2k}{3}} \underline{e}_R \tag{15}$$

where $\overline{\underline{u}_l}$ is the mean flow velocity, k is the turbulent kinetic energy, and $\underline{e}_R$ is a randomly oriented unit vector.
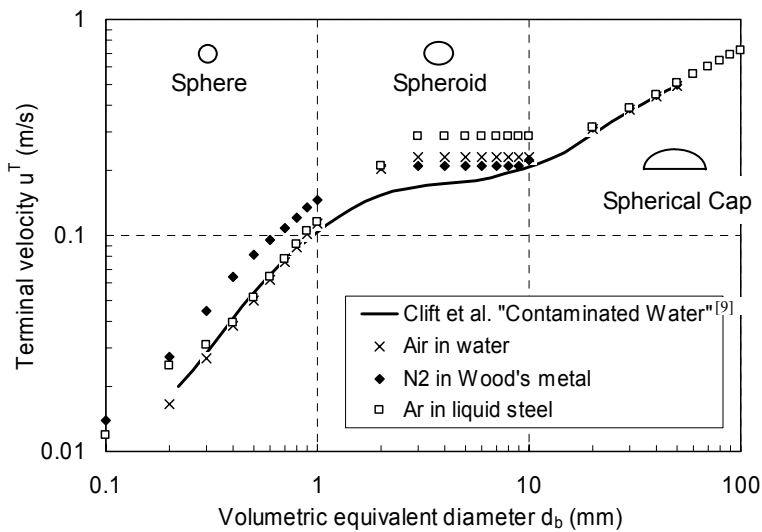

Figure 1. Terminal velocity and shape of bubble in various systems calculated from the drag coefficient in eq. (11)
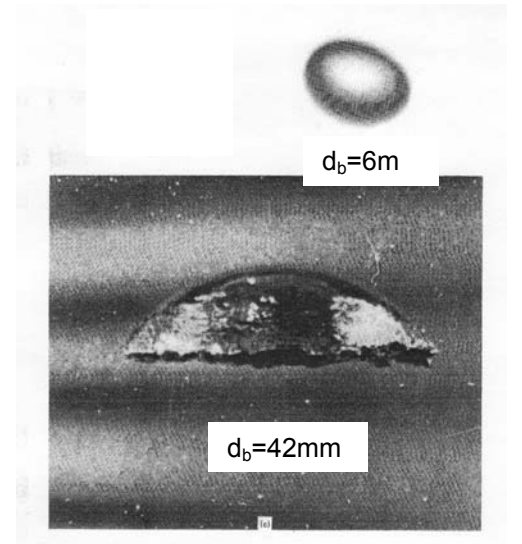

Figure 2. The shape of air bubbles in water[9]

Gas Density and Volume Fraction

The density and the diameter of the bubble is calculated at each position according to the local static pressure and the temperature, using the ideal gas law as follows:

$$\rho_{b,i} = \rho_{0b} \frac{p_0 + \rho_l g(H - y_i)}{p_0} \frac{T_0}{T} \tag{16}$$

$$\rho_b^{bottom} = \rho_{0b} \frac{p_0 + \rho_l gH}{p_0} \frac{T_0}{T} \tag{17}$$

$$d_{b,i} = \sqrt[3]{\frac{\rho_b^{bottom}}{\rho_{b,i}}} \, d_b^{bottom} = \sqrt[3]{\frac{p_0 + \rho_l gH}{p_0 + \rho_l g(H - y_i)}} \, d_b^{bottom} \tag{18}$$

The subscript 0 refers to the standard temperature and pressure (STP) of 273.15K and 101,325Pa. H is the bath depth, y_i is the vertical coordinate starting from the bottom of the ladle, and the superscript "bottom" means the bottom of the ladle where gas is injected. Because the density difference between at the bottom and at the top is small in a water experiment, this effect is usually neglected for simulating flow in water models. In molten metal, however, the volume expansion of a bubble along the vertical direction due to the static pressure change is not negligible. For example, if the bath depth of steel is 3m, the gas density at the bottom is three times higher than the density at the top surface. Furthermore, the high operating temperature in the molten steel causes a decrease in the gas density of roughly six times, relative to room temperature. Thus, accurate corrections to the density and diameter of the bubbles are incorporated into the simulation.

Bubble and liquid volume fraction is calculated as follows, and included into the liquid phase equation.

$$\alpha_b = \frac{1}{\Delta V_{cell}} \sum_i^{N_{b,cell}} \frac{Q_{b,i}^s \Delta t}{\rho_{b,i}} \tag{19}$$

$$\alpha_l = 1 - \alpha_b \tag{20}$$

Bubble Size Distribution

The bubble size distribution is also taken into account in this model. The number distribution of bubble diameter is expressed experimentally with the following logarithmic normal function,[10]

$$P = P_m \exp\left(\frac{-\left[\ln(d_b) - \ln(d_b^m)\right]^2}{2\left[\ln(s)\right]^2} \right) \tag{21}$$

where P_m is the maximum relative probability, d_b^m is the bubble diameter with the maximum number distribution, and s is the standard deviation. Because the small bubbles result from the break up of a large "parent" bubble, it is reasonable that d_b^m is assumed to depend on the bubble size at the inlet nozzle, according to Davidson et al.[11],

$$d_b^N = 1.381 \left(\frac{Q_b^2}{g} \right)^{0.2} \tag{22}$$

and the following relationship is assumed,

$$d_b^m = 0.04 \left(\frac{Q_b^2}{g} \right)^{0.2} + 0.0007 \tag{23}$$

The value of s is assumed to be 0.026m, based on the calibration to match the Wood's metal experiment[10].

Coupling Lagrangian and Eulerian Calculations

The coupling together of the Lagrangian bubble motion calculation and the Eulerian fluid flow calculation is performed by a natural alternating step-by-step method during the transient solution. Firstly, bubbles are injected into the domain from the nozzle location, and the bubble trajectories are calculated by integrating the Lagrangian equations for one computational time step. The drag force, buoyancy force, virtual mass force, lift force, and the pressure gradient force are calculated, and eq. (10) is solved to obtain each bubble trajectory. During the trajectory calculation, the interaction force in eq. (3) and the source of turbulent kinetic energy due to bubble motion (eq. (9)) are stored for each computational cell. The position, velocity, density, and diameter of each bubble are updated at each time step. Bubble and liquid phase fractions are calculated from eq. (19) and (20) and stored in the computational cell. Secondly, the Eulerian liquid phase equations are solved. It should be noted that in the Eulerian calculation, $Q_b^s \Delta t$, the bubble stream flow rate (kg/s) multiplied by the time step (s), is used instead of the actual bubble mass (kg) based on the gas density and the bubble diameter, while the actual bubble mass is used in Lagrangian trajectory calculation. Enforcing a total gas mass balance enables the

number of bubbles calculated in the Eulerian domain to not necessarily match with the actual number of bubbles. This makes it possible for large bubbles to be split into several smaller bubbles (with the same total mass) using several injection streams, which enables the computational cell volume to be small enough for accuracy, yet larger than the bubble size, which helps to avoid convergence problems.

MODEL 2. INCLUSION ATTACHMENT TO A BUBBLE

An axisymmetric model is developed for turbulent fluid flow during flotation of an individual bubble, the random motion of an inclusion through this flow field, and the collision and possible attachment of the inclusion to the bubble. Statistical analysis is performed from the results of thousands of simulations to determine inclusion attachment probabilities.

Bubble Morphology
As shown in Figure 2, the bubble shape changes with its diameter, evolving from sphere, to spheroid, to spherical cap with increasing diameter. In the spheroidal region, the aspect ratio is given as a function of Eotovos number,[12]

$$e = 1 + 0.163 Eo^{0.757} \tag{24}$$

$$Eo = \frac{d_b^2 g (\rho_l - \rho_b)}{\sigma} \tag{25}$$

where e is the aspect ratio, d_b is the volumetric "equivalent" diameter which is defined as the diameter of the sphere that has the same volume as the distorted bubble's volume V_b.

$$d_b = \sqrt[3]{\frac{6}{\pi} V_b} \tag{26}$$

As the bubble size becomes larger, its aspect ratio becomes larger, and finally the bubble's shape transforms into a spherical cap. Davis and Taylor[13] showed that for a spherical cap bubble, the drag coefficient is independent of Reynolds number and takes the value of 8/3. They also determined the relationship between the terminal velocity and the curvature radius of the spherical cap as follows,

$$u_T = \frac{2}{3} \sqrt{gR} \tag{27}$$

where u_T is the terminal velocity of the bubble, and R is the radius of curvature of the spherical cap.
Substituting the constant drag coefficient = 8/3 into eq. (10), and equating the drag force and the buoyancy force,

$$\frac{2\rho_l}{\rho_b d_b} u_T^2 = \frac{(\rho_l - \rho_b)}{\rho_b} g \tag{28}$$

From (27) and (28), and assuming ρ_b/ρ_l is negligibly small, R and d_b are related by,

$$R = \frac{9}{8} d_b \tag{29}$$

The volume of a spherical cap with radius R and center angle θ is,

$$\frac{\pi}{3} R^3 (2 - 3\cos\theta + \cos^3\theta) = \frac{\pi}{6} d_b^3 \tag{30}$$

Substituting (30) into (29), the center angle $\theta = 50.59°$ is determined, which is in good agreement with experimental measurements[13], which range from 46° to 64°.

Inclusion Attachment Probability
Inclusion attachment probability is defined as the ratio between the number of inclusions captured on the bubble surface and the number of inclusions contained in the volume swept by the moving bubble. This can be simply expressed in terms of a critical column diameter, based on the following ratio of surface areas or diameters[14],

$$P_A = \frac{\dfrac{\pi d_c^2}{4}}{\dfrac{\pi (d_b + d_p)^2}{4}} = \left(\frac{d_c}{d_b + d_p}\right)^2 \tag{31}$$

where P_A is the attachment probability, d_c is the critical diameter in which the inclusion attaches to the bubble, d_b is the bubble diameter, and d_p is the inclusion diameter. The subscript "p" means inclusion (particle). The number of inclusions attached to the bubble surface N_p^a is then calculated as,

$$N_p^a = P_A \frac{\pi (d_b + d_p)^2}{4} C_p^V \Delta l \qquad (32)$$

where C_p^V is the number of inclusions per unit volume (m^{-3}), and Δl is the path length of the bubble (m).

The criterion for determining the critical diameter d_c must incorporate two phenomena: one is collision and the other is attachment. In this study, the inclusion trajectory through the flow field around the bubble is calculated numerically using the same Lagrangian method as the bubble trajectory calculation in the ladle flow (eq. (10)). If the trajectory of the inclusion enters within the layer of $d_p/2$ thickness from the bubble surface, it is taken as "collided and sliding on the surface". The sliding time is defined as the duration while the inclusion is traveling within this layer.

When an inclusion collides with the bubble surface, a thin liquid film layer is formed between the bubble surface and the inclusion, and the inclusion slides along this film. If the film ruptures before the inclusion moves away from the bubble, then the bubble will attach to the surface. The film rupture time t_f is calculated from the following equations,[14]

$$t_f = \frac{64}{3} \mu_l \frac{\alpha^2}{4 \sigma h_{cr}^2} d_p^3 \qquad (33)$$

$$\alpha = \arccos\left(1 - 1.02 \left(\frac{\pi d_p \rho_p |\underline{u}_p - \underline{u}_b|^2}{12 \sigma_{lb}} \right)^{\frac{1}{2}} \right) \qquad (34)$$

$$h_{cr} = 2.33 \times 10^{-8} [1000 \sigma_{lb} (1 - \cos\theta_p)]^{0.16} \qquad (35)$$

where θ_p is the contact angle of the liquid on the inclusion surface. The value of the film rupture time is very small for small nonwetting inclusions. Even for wetting inclusions, such as silica inclusions, t_f is about 7×10^{-4}s for 100μm diameter, and 2×10^{-7}s for 10μm diameter, whereas the sliding time is generally 10^{-3} to 10^{-1} seconds. Therefore, small inclusions attach almost instantly upon hitting the bubble surface.

Statistical Approach Defining Attachment Probability in Turbulence

Most previous studies on inclusion attachment probability[14-16] are based on trajectory calculations along flow streamlines, and the effect of turbulence is neglected. Significant turbulence is associated with the macroscale flow pattern of many processes, and should not be confused with the local flow effects related to the bubble and particle motion, which can range from laminar to turbulent, according to the particle Re number. One difficulty in turbulent flow conditions is that the critical diameter d_c cannot be defined. Because inclusion motion has chaotic behavior in a turbulent flow field, an inclusion from within the theoretically defined critical diameter d_c may not ever get close to the bubble, while an inclusion from outside of d_c may wander into the bubble vicinity and attach. Thus, in this study, a more general statistical method to calculate the inclusion attachment probability in a turbulent field is developed.

Firstly, in the case of low turbulence (k≤10^{-3}m^2/s^2), inclusions are injected from an upstream plane. The distance between the bubble center and this injecting plane is set to $5d_b$, which can be considered far enough away for the bubble to properly interact with the flow field, based on potential flow theory. The inclusion concentration on the injecting plane is set to a constant, C_p^S. Then inclusion trajectories are calculated including turbulent random walk by solving eqs. (10) and (15), and the number of inclusions attaching to the bubble N_p^a are counted. The particle attachment probability P_A is calculated as follows.

$$P_A = \frac{N_p^a}{C_p^S \frac{\pi (d_b + d_p)^2}{4}} \qquad (36)$$

Because the surface inclusion concentration C_p^S equals the number of inclusions passing through the unit surface area along the particle trajectory,

$$C_p^S = C_p^V \Delta l \qquad (37)$$

Thus, eqs. (32) and (36) are the equivalent.

Secondly, in the case of higher turbulence (k≥10^{-2}m^2/s^2), if the turbulent fluctuation component of the particle velocity given by eq. (15) is near to or higher than the bubble mean velocity, then inclusions may approach the bubble from any direction, even from behind the bubble. Thus, the above approach using a plane of injected particles is not applicable. Instead, inclusions are injected from the surface of a sphere centered around the bubble, and the number of inclusions attaching to the bubble is counted as before. The radius R of the spherical injecting surface is set to $5d_b$ using the same reasoning as above, and the particle attachment probability is again obtained from eqs. (36) and (37).

MODEL 3. INCLUSION REMOVAL BY BUBBLES IN LADLE FLOW

Inclusion transport in the turbulent flow field is modeled by the following equation for transient diffusion and transport of a continuum species,

$$\frac{\partial}{\partial t}\left(\alpha_l \rho_l C_p^M\right) + u_x \frac{\partial\left(\alpha_l \rho_l C_p^M\right)}{\partial x} + \left(u_y + u_p^T\right)\frac{\partial\left(\alpha_l \rho_l C_p^M\right)}{\partial y} + u_z \frac{\partial\left(\alpha_l \rho_l C_p^M\right)}{\partial z} = \nabla\left(\frac{\alpha_l \mu_t}{Sc}\right)\nabla C_p^M - S_p \tag{38}$$

where C_p^M is the inclusion number concentration per unit liquid mass (kg^{-1}),

$$C_p^M = C_p^V \Big/ \rho_l \tag{39}$$

u_p^T is the terminal floating velocity of the inclusion due to its buoyancy, Sc is the turbulent Schmidt number for mixing which is set to 1 in this study, and S_p is the removal rate by attachment to bubbles, given by the following equation,

$$S_p = \frac{1}{\Delta V_{cell}} \sum_i^{N_b^{cell}} \left(P_{A,i}\left(d_p, d_b, k\right) S_R \frac{\pi\left(d_{b,i} + d_p\right)^2}{4} \alpha_l \rho_l C_p^M \left|u_l - u_{b,i}\right| \Delta t \right) \tag{40}$$

The term inside the large parenthesis in eq. (40) is the number of inclusions attached to each bubble, the same as eq. (32). The particle attachment probability P_A is given as a function of inclusion size, bubble size, and turbulent kinetic energy, from the results of model 2. S_R is the fraction of the bubble surface area which is not already occupied by attached inclusions,

$$S_R = \frac{\pi d_b^2 - N_{p,i}\frac{\pi d_p^2}{4}}{\pi d_b^2} \tag{41}$$

where $N_{p,i}$ is number of inclusions already attached to the surface. As a bubble collects inclusions and $N_{p,i}$ becomes larger, the effective bubble surface area decreases, and is finally saturated with inclusions.

The terminal velocity of an inclusion u_p^T is calculated by the following equations for small particle Reynolds number.

$$\frac{3 C_D \operatorname{Re}}{4 \rho_p d_p^2} u_p^T = \frac{\pi d_p^3}{6}\left(\frac{\rho_l - \rho_p}{\rho_p}\right)g \tag{42}$$

$$C_D = \frac{24}{\operatorname{Re}} \qquad (\operatorname{Re} < 1) \tag{43}$$

From eq. (42) and (43),

$$u_p^T = \frac{\rho_l - \rho_p}{18\mu} d_p^2 g \tag{43}$$

In this study, the composition of the inclusions is assumed to be pure Al$_2$O$_3$, and the dissolved oxygen content is assumed to be negligible. The relationship between oxygen content C_O and the inclusion number concentration C_p^M is thus,

$$C_O = \frac{\pi}{6} d_p^3 \rho_p \frac{3 M_O}{M_{Al_2O_3}} C_p^M \tag{44}$$

where M_O and $M_{Al_2O_3}$ are the molecular mass of oxygen and Al$_2$O$_3$.

COMPUTATIONAL DETAILS

The computational models are evaluated using FLUENT ver. 6.1.22[17] on a Windows XP PC with Pentium®4 3.20 GHz CPU and 2 Gbyte RAM. Because several of the critical equations in the models (explained in the previous sections) are not supported by FLUENT, user defined functions (UDF) written in C language have been developed and incorporated into FLUENT. The model configuration is shown in Figure 3.

For the ladle flow simulation, a three-dimensional transient calculation is performed in a domain containing about 40,000 hexahedral computational cells. The second-order implicit time discretization scheme is used for the unsteady calculation with convergence

criteria set to 10^{-4} relative error for the residuals of the continuity equation, the momentum equation, and the transport equation of k and ε.

To validate the accuracy of the simulation, the Wood's metal experiment by Xie and Oeters[6] is modeled first, and the calculated flow field and gas volume fraction is compared with the experimental value. This case employs a 0.40m diameter and 0.37m height cylindrical domain with central gas injection corresponding to the experimental vessel. A time step size of 0.002 second is chosen, and 4,000 time steps corresponding to 20 seconds of ladle flow are calculated. The average fluid velocity, turbulent kinetic energy, and its dissipation rate over the domain are monitored to evaluate development of the flow field. The flow became fully developed after about 10 seconds, and the time-average of the values between 10 second and 20 second are used for comparison with the experimental data. This time averaging technique is important because the flow field is unsteady by its nature, and the plume position fluctuates with time even after it reaches a fully developed state.

After evaluating the model, the flow field in the steel ladle containing 133 tonnes of liquid steel is modeled. The shape of the ladle is a tapered cylinder, whose height is 3m, and whose diameter is 3m at the top and 2.7m at the bottom. A single off-centered porous plug injecting Ar gas is located at the half-radius at the bottom wall. The time step is chosen as 0.02 second, and 4,500 time steps corresponding to 90 seconds of ladle flow are computed. The flow field becomes fully developed in 60 seconds, and the time average of the results between 60 and 90 seconds are used for inclusion calculations.

The calculation of inclusion attachment to bubble is done in a two-dimensional axisymmetric domain. The domain size is $200d_b$ in length and $100d_b$ in height with a bubble located at the center of the symmetry axis. It is rescaled and distorted according to the bubble size and aspect ratio for spherical and spheroidal bubbles. An axisymmetric domain is also designed for the spherical cap bubble shape and is also rescaled according to the bubble size. The steady flow field is calculated with the convergence criteria of 10^{-5} for residuals. Uncoupled inclusion trajectories are computed through the time-averaged flow field. During each inclusion trajectory calculation, the attachment criterion is checked using a UDF, and the number of attached inclusions is output on the screen.

Finally, the inclusion concentration calculation is done using the results of the flow field and inclusion attachment probabilities. The unsteady evolution of inclusion concentration is simulated in the time-averaged flow and turbulence fields. The time step is chosen as 0.2 second, and 3000 time step corresponding to 600 sec of bubbling time is computed. The convergence criterion for inclusion concentration is set to 10^{-5} for residuals.

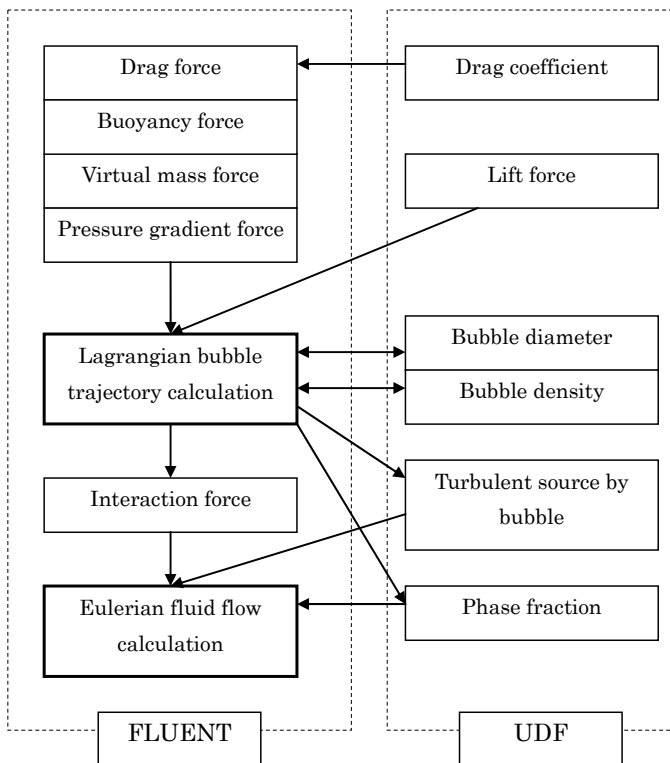A list of the constants used in the calculation is provided in Table I.

Figure 3. Model configuration

Table I List of constants

Material	Property	Value	Unit
Liquid steel	Density	7000	kg/m^3
	Viscosity	0.0067	kg/ms
	Surface tension	1.4	N/m
	Temperature	1850	K
Wood's metal	Density	9560	kg/m^3
	Viscosity	0.00326	kg/ms
	Surface tension	0.46	N/m
	Temperature	373.15	K
Argon	Density (STP)	1.784	kg/m^3
Nitrogen	Density (STP)	1.2506	kg/m^3
Alumina	Density	2800	kg/m^3

MODEL VALIDATION

The model is first applied to simulate fluid flow and bubble motion in a one tenth scale-size ladle of Wood's metal, where accurate experimental measurements were available[6]. The calculated flow field and the contour of gas fraction in a vertical section of the ladle are shown in Figures 4 and 5. The gas flow rate is 2×10^{-4} m^3/s in STP. A comparison between experimental and calculated time-averaged liquid velocity along the vertical direction (y direction) is plotted in Figure 6, and the corresponding comparison of gas fraction is in Figure 7. The injected gas forms a plume which is upward stream of mixture of liquid and gas bubbles. The calculated flow velocity and gas fraction are in reasonably good agreement. The peak velocity of the plume is reproduced well. The width of the computed plume, however, is wider than the experimental one.
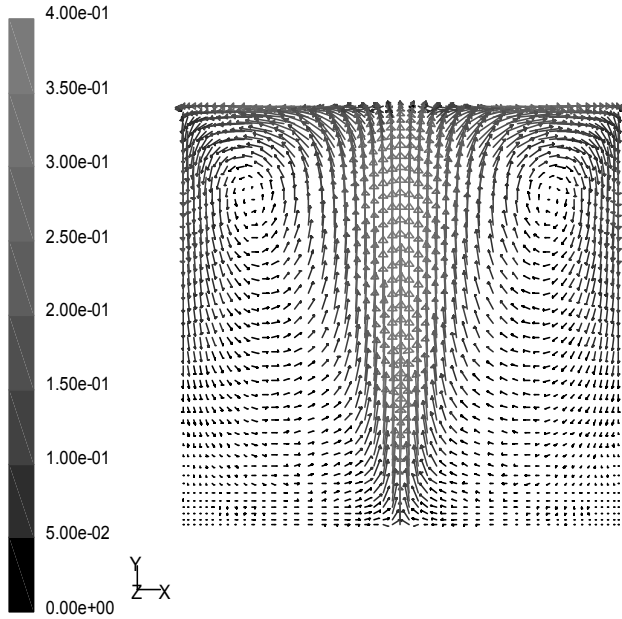
Figure 4 Time averaged flow field of
Wood's metal experiment (FLUENT output)
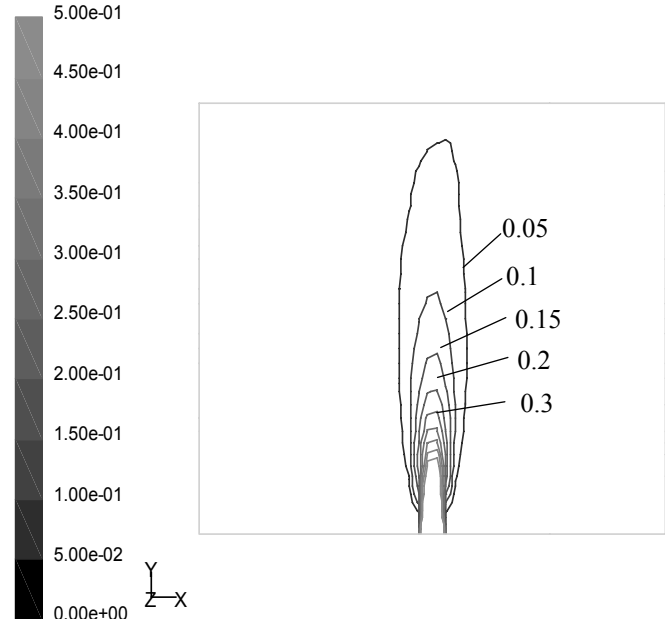
Figure 5 Time averaged gas volume fraction in
Wood's metal experiment (FLUENT output)
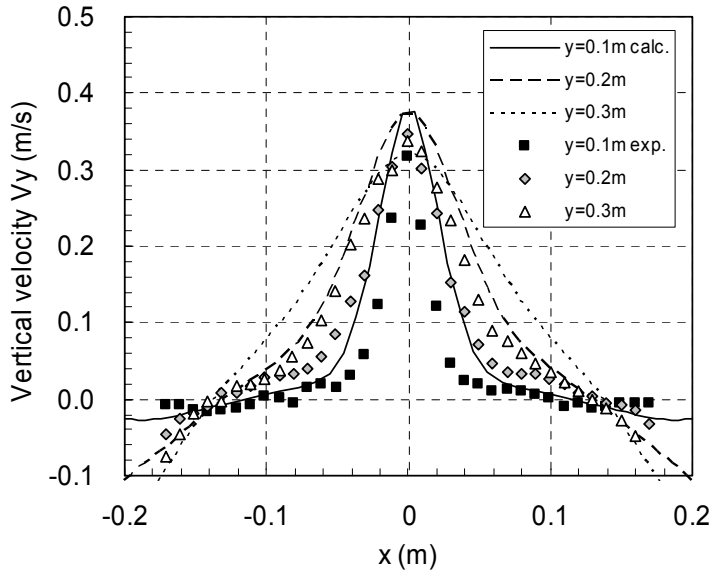
Figure 6 Comparison of vertical velocity between
simulation and experiment
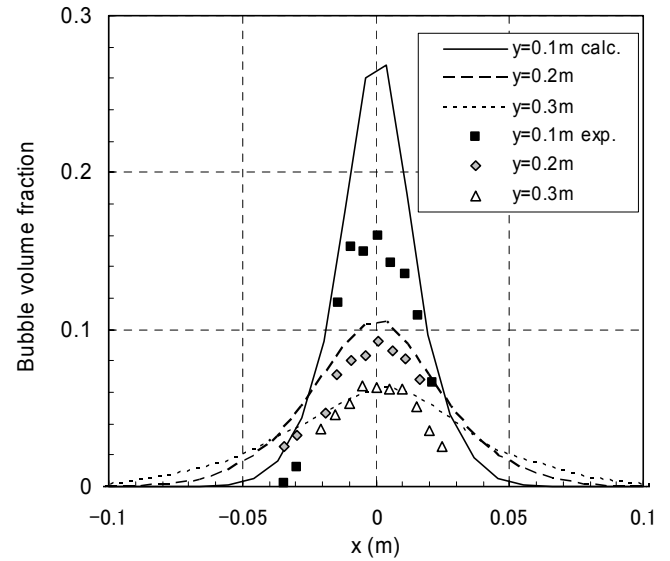
Figure 7 Comparison of bubble volume fraction
between simulation and experiment

Flow Field in Steel Ladle
The calculated flow field in the 133-ton steel-refining ladle with off-centered bottom gas injection is shown in Figure 8. The gas flow rate is $5 \times 10^{-3} m^3/s$ at STP. Unlike central gas injection, the plume bends toward the ladle wall because of the returning flow, and a large recirculation pattern in the ladle is formed. Figure 9 shows contours of the turbulent kinetic energy. The turbulent kinetic energy in most of the plume region is about $0.1 m^2/s^2$, and therefore the value of turbulent kinetic energy is set to $0.1 m^2/s^3$ in later inclusion removal calculation.
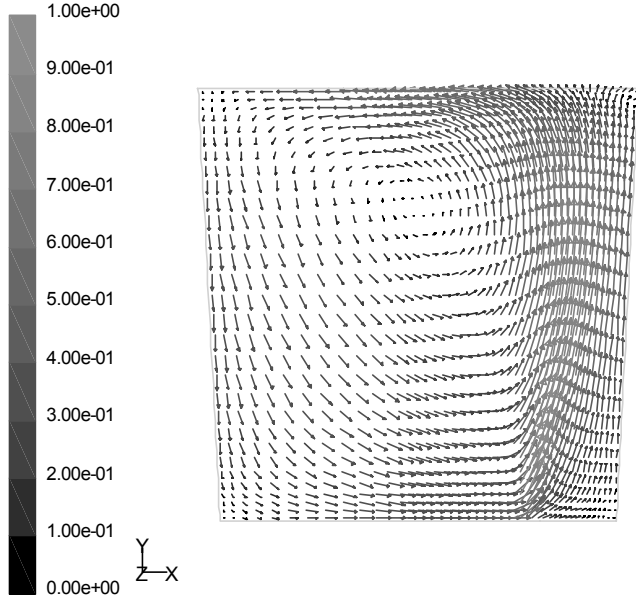
Figure 8 Calculated flow field in ladle with off-centered Ar bubbling (FLUENT output)
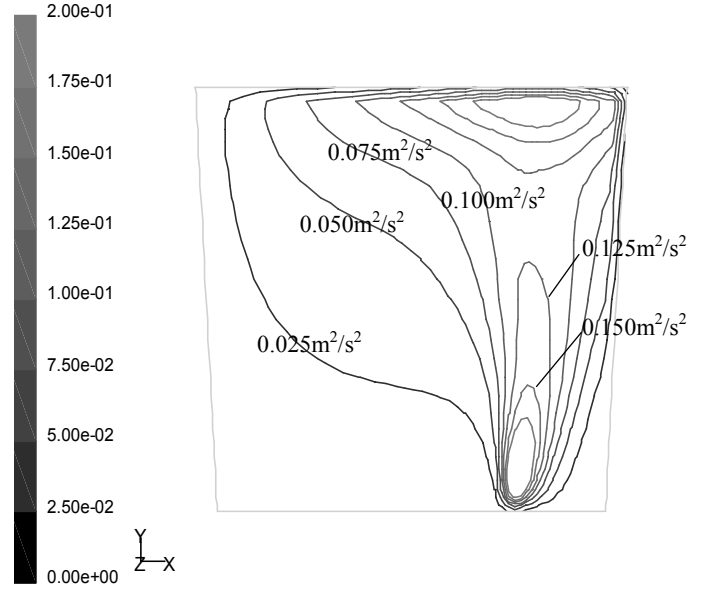
Figure 9 Calculated turbulent kinetic energy distribution (FLUENT output)

Particle Attachment Probability
Figure 10 and Figure 11 shows examples of the particle trajectory calculation toward a spherical cap bubble considering the turbulent random walk effect in low turbulence ($k=10^{-6} m^2/s^2$) and high turbulence ($k=0.1 m^2/s^2$) flow fields. In the low turbulent case (Figure 10), the plane injection method is applied, and in the high turbulent case (Figure 11), the spherical injection method is applied. The surface injection concentration multiplied by the swept area, $C_p^S \dfrac{\pi (d_p + d_b)^2}{4}$ is set to 10 in Figure 10 and 1 in Figure 11 to show the concept, but the value is set to 1000 for planer injection and 100 for spherical surface injection in actual attachment probability calculations, and the average value out of 10 trials is adopted as the final result for each condition. This number corresponds to 40,000 to 400,000 individual inclusions for each simulation.

In Figure 10, some inclusions are trapped in the recirculation zone behind the bubble. These trapped inclusions are considered to float with the bubble, and finally are removed if they accompany the bubble to the liquid surface. Therefore, the number of trapped inclusions is also counted, and included into the particle attachment probability. The criterion of duration for the inclusion to be trapped is set to 3 second, which is estimated to be the average bubble residence time. Figure 11 shows that in cases of high turbulence, the turbulent fluctuation velocity can be higher than the average bubble rising velocity, so inclusions from the sides or even from behind can approach and have a chance to attach to the bubble.

Figure 12 shows the calculated inclusion attachment probability for various bubble size d_b and turbulent kinetic energy k. The inclusion diameter d_p is fixed to 100μm. Without the turbulent random walk model, the inclusion attachment probability becomes smaller with increasing bubble diameter. But when turbulent random motion is taken into account, the attachment probability becomes one or two orders of magnitude higher for the larger bubble than the same case without random motion, and the dependency on bubble diameter decreases. Increasing the level of turbulent kinetic energy k also increases the inclusion attachment probability. The case of

$k=0.1m^2/s^2$ is examined more, because it is the turbulent kinetic energy in plume region as shown in Figure 9. This result is used for the inclusion transport calculation.

Figure 13 is a re-plot of the case of $k=0.1m^2/s^2$ in Figure 12. The curved lines are the result of parameter fitting that gives the inclusion attachment probability as a function of d_b, and the function is incorporated into eq. (40) to obtain the inclusion removal rate in the ladle simulation. The two curves correspond to spherical and spheroidal bubbles and to spherical cap bubbles respectively. The inclusion attachment probability decreases with increasing bubble diameter by nature, but as the bubble diameter increases, the aspect ratio changes and the surface area swept by the bubble increases. This effect causes the first minimum. The second minimum, in the spherical cap region, is related to particle entrapment in the recirculation zone. The number of inclusions trapped in the recirculation zone increases with increasing the bubble diameter and decreasing the turbulent kinetic energy, because the size of the recirculation zone increases for large bubbles and low turbulence.
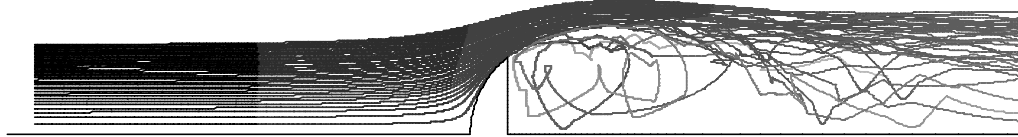

Figure 10 Inclusion trajectories in low turbulence (d_b=100mm, d_p=100μm, $k=10^{-6}m^2/s^2$)

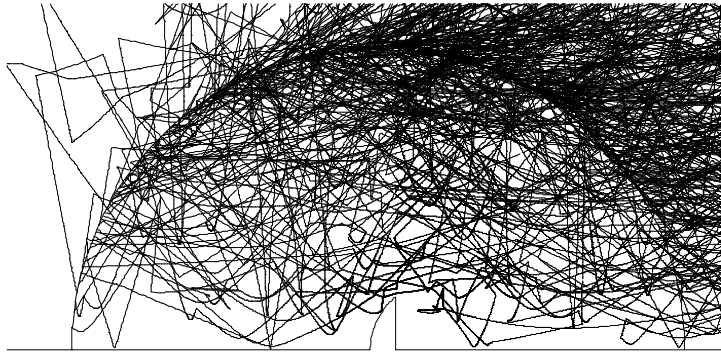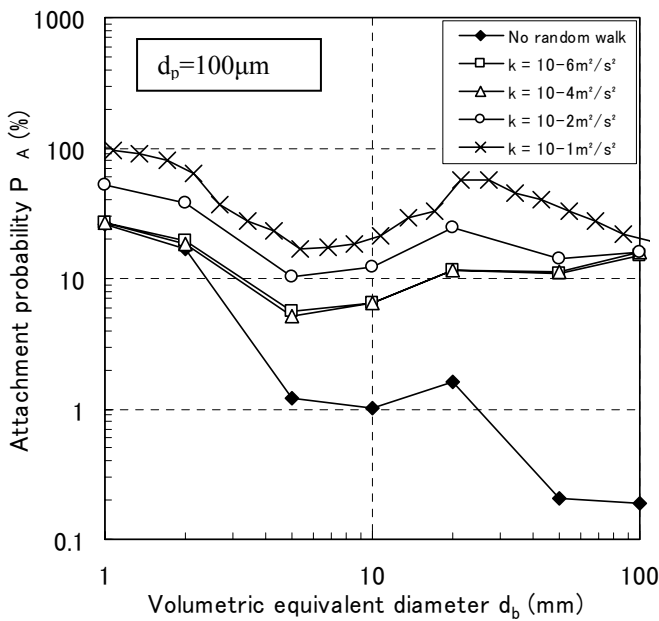Figure 11 Inclusion trajectories in high turbulence (d_b=20mm, d_p=100μm, $k=0.1m^2/s^2$)

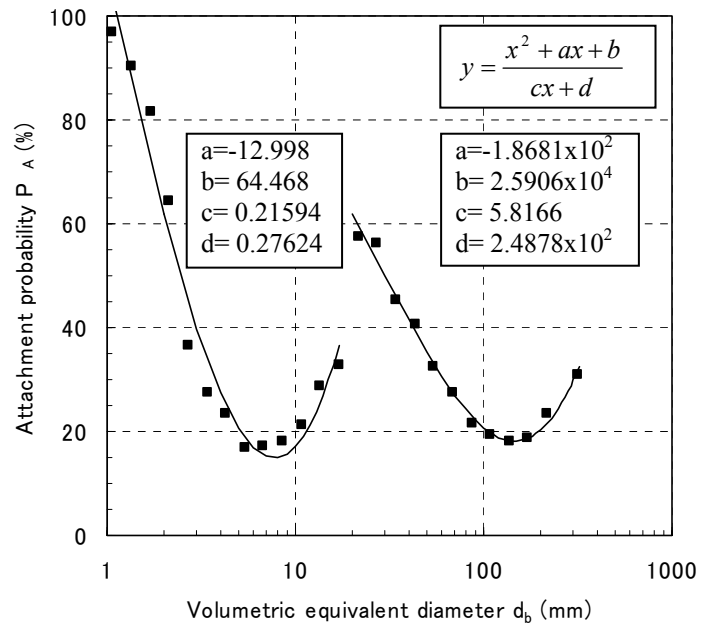

Figure 12 Particle attachment probability with turbulent random motion

Figure 13 Fitting curve of attachment probability for d_p=100μm and $k=0.1m^2/s^2$

Inclusion Removal in Ladle

Figure 14 shows the evolution of oxygen concentration and deoxidization rate constant K_o with bubbling time. The initial oxygen concentration is set to 50 ppm, and it decreases only by inclusion removal by attachment to bubble. The rate constant K_o is defined as,

$$\frac{dC_O}{dt} = -K_O C_O \tag{45}$$

assuming first order reaction.

Figure 15 shows the relationship between K_o and stirring energy for various practical processes. The data points obtained in this work are also plotted. The present model predictions of 0.16-0.24 min^{-1} fall barely within the upper limit of measurements for similar Ar-gas stirred refining processes. Many possible reasons exist for this. Firstly, the inclusion size distribution found in the real process may produce attachment probabilities that are lower than that for the constant diameter particle of 100μm assumed in this study. Secondly, the kinetics of entrainment of the inclusion-laden bubbles into the top-surface slag layer is ignored. Thirdly, other inclusion sources, such as ladle refractory erosion and reoxidation from the slag or atmospheric exposure are neglected in this work.
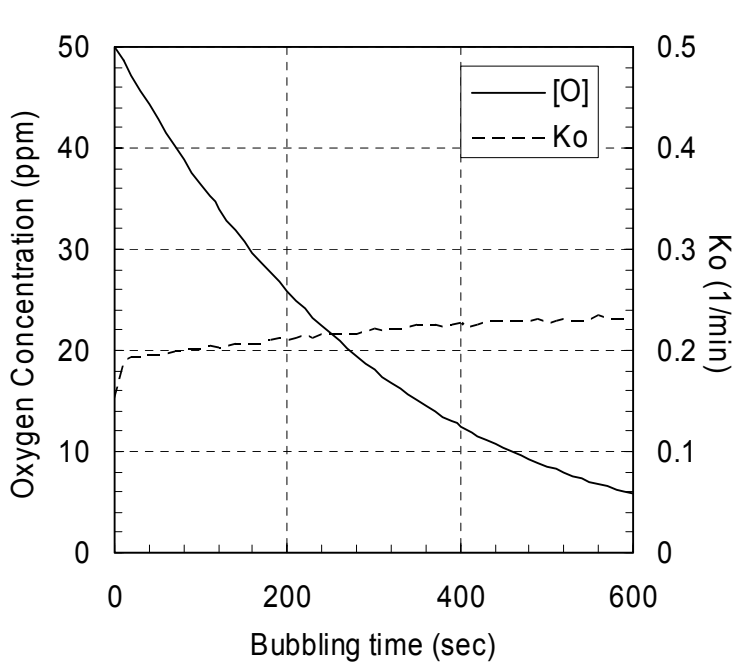

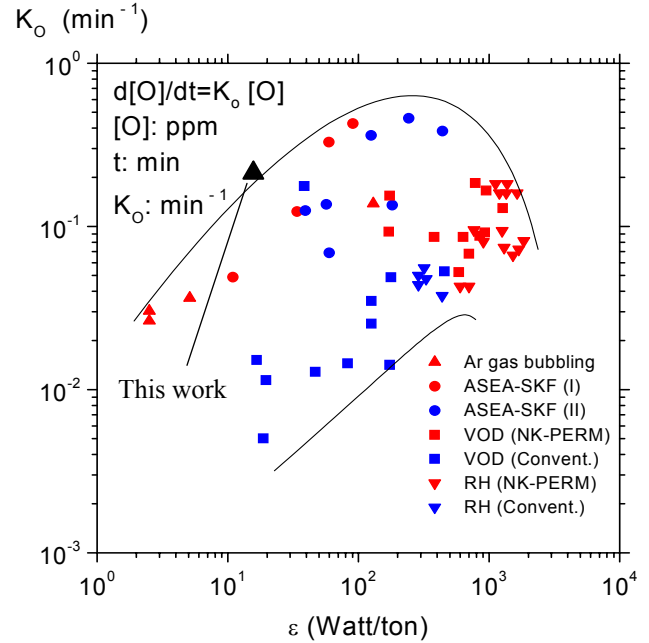Figure 14 Oxygen concentration and rate constant changing with bubbling time

Figure 15 Comparison of Ko with various processes[18]

CONCLUSION

An Eulerian-Lagrangian model of three-dimensional unsteady multiphase flow in gas stirred metallurgical vessels has been developed and applied to simulate fluid flow, bubble behavior, and inclusion removal in a bottom-injection, gas-stirred steel refining ladle. The important effects of spatially-varying phase fractions, gas volume expansion according to the static pressure change, lift force, and turbulence generated by the bubbles are included using "user-defined-functions" in FLUENT. The calculated flow field and gas volume fraction matches well with an experiment in Wood's metal.

The probability of inclusion attachment to large spheroidal or spherical cap bubbles in a turbulent flow field is determined for the first time. Considering random turbulent motion, the attachment probability is 10 to 100 times higher than the conventional method neglecting turbulent random effect. Particles can also be trapped in the recirculation zone in the wake behind a large spherical cap bubble.

Finally, the effect of gas bubbling on decreasing oxygen concentration is calculated. The deoxidization rate constant K_o is just within the range of data measured for various refining process. The models are ready to be augmented with other phenomena and applied to the understanding and design of metallurgical refining vessels.

REFERENCES

1. J. Peter, K. D. Peaslee and D. G. C. Robertson, "Study of Current Steelmaking Practices to Evaluate the Viability of Continuous Steelmaking," *AISTech 2004 Iron and Steel Conference Proceedings*, Vol.1, AIST, Warrandale, PA, (Nashville, TN, September 2004), 2004, pp. 1071-1083.
2. J. Peter, K. D. Peaslee and D. G. C. Robertson, "Introduction of a Novel, Scrap-Based, Fully Continuous Steelmaking Process," *AISTech 2005 Iron and Steel Conference Proceedings*, AIST, Warrandale, PA, (Charlotte, NC, May 2005), 2005, in press.
3. L. Zhang, J. Aoki, B. G. Thomas, J. Peter and K. D. Peaslee, "Designing a New Scrap-Based Continuous Steelmaking Process using CFD Simulation," *ICS 2005 - The 3rd International Congress on the Science and Technology of Steelmaking*, AIST, Warrandale, PA, (Charlotte, NC, May 2005), 2005, in press.
4. D. Guo and G. A. Irons, "Modeling of Gas-Liquid Reactions in Ladle Metallurgy: Part II. Numerical Simulation," *Metallurgical and Materials Transactions B*, Vol. 31B, December 2000, pp. 1457-1464.
5. S. T. Johansen and F. Boysan, "Fluid Dynamics in Bubble Stirred Ladles: Part II. Mathematical Modeling," *Metallurgical Transactions B*, Vol. 19B, October 1988, pp. 755-764.
6. Y. Xie and F. Oeters, "Experimental Studies on the Flow Velocity of Molten Metals in a Ladle Model at Centric Gas Blowing," *Steel Research*, Vol. 63, No. 3, 1992, pp. 93-104.
7. J. T. Kuo and G. B. Wallis, "Flow of Bubbles through Nozzles," *Int. J. Multiphase Flow*, Vol. 14, No. 5, 1988, pp. 547-564.
8. S. W. Beyerlein, R. K. Cossmann and H. J. Richter, "Prediction of Bubble Concentration Profiles in Vertical Turbulent Two-Phase Flow," *Int. J. Multiphase Flow*, Vol. 11, No. 5, 1985, pp. 629-641.
9. R. Clift, J. R. Grace and M. E. Weber, "Shapes of Rigid and Fluid Particles," *Bubbles, Drops, and Particles*, Academic Press, New York, NY, 1978, pp. 16-29.
10. Y. Xie, S. Orsten and F. Oeters, "Behaviour of Bubbles at Gas Blowing into Liquid Wood's Metal," *ISIJ International*, Vol. 32, No. 1, 1992, pp. 66-75.
11. J. F. Davidson and B. O. G. Schüler, "Bubble Formation at an Orifice in an Inviscid Liquid," *Trans. Instn Chem. Engrs.*, Vol. 38, 1960, pp. 335-342.
12. R. M. Wellek, A. K. Agrawal and A. H. P. Skelland, "Shape of Liquid Drops Moving in Liquid Media," *A. I. Ch. E. Journal*, Vol. 12, No. 5, September 1966, pp. 854-862.
13. R. M. Davis and G. Taylor, "The Mechanics of Large Bubbles Rising through Extended Liquids and through Liquids in Tubes," *Proceedings of the Royal Society of London, Series A, Mathematical and Physical Sciences*, Vol. 200, No. 1062, February 1950, 375-390.
14. L. Zhang and S. Taniguchi, "Fundamentals of Inclusion Removal from Liquid Steel by Bubble Flotation," *International Materials Reviews*, Vol. 45, No. 2, 2000, pp. 59-82.
15. L. Wang, H.-G. Lee and P. Hayes, "Prediction of the Optimum Bubble Size for Inclusion Removal from Molten Steel by Flotation," *ISIJ International*, Vol. 36, No. 1, 1996, pp. 7-16.
16. C. M. Phan, A. V. Nguyen, J. D. Miller, G. M. Evans and G. J. Jameson, "Investigations of Bubble-Particle Interactions," *INt. J. Miner. Process*, Vol. 72, 2003, pp. 239-254.
17. FLUENT inc., Lebanon, NH.
18. L. Zhang and B. G. Thomas, "Alumina Inclusion Behavior during Steel Deoxidation," *7t^h European Steelmaking Conference*, Associazione Italiana di Metallurgia, Milano, Italy, (Venice, Italy, May 26-29, 2002), 2002, pp. 2.77-2.86.